Validation of Ab-Initio-Predicted Magnetic Anisotropies and Magneto-structural Correlations in Linear Hetero-trinuclear Dy^{III}-Ni$^{II}_2$ Compounds

Peter Comba,*[a, b] Markus Enders,[a] Michael Großhauser,[a] Markus Hiller,[a] Rüdiger Klingeler,*[c, d] Changhyun Koo,[c] Dennis Müller,[a, b] Gopalan Rajaraman,[e] Abinash Swain,[e] Msia Tavhelidse,[c] and Hubert Wadepohl[a]

Abstract: Reported are single crystal SQUID and single crystal high-frequency/high-field EPR data of a trinuclear complex with a rare six-coordinate coordination sphere of a Dy^{III} center coupled to two terminal six-coordinate Ni^{II} ions. The analysis of the single crystal spectroscopic parameters allows for an accurate description of the ground state wavefunction. The experimental analysis is supplemented by the analysis of the paramagnetic NMR spectra, allowing for a thorough description of the Dy^{III} center. The experimental data are interpreted on the basis of an ab initio ligand field analysis, and the computed parameters are in good agreement with the experimental observations. This supports the quality of the theoretical approach based on a pseudo-spin Hamiltonian for the electronic ground state. Further support emerges from the ab initio ligand field theory based analysis of a structurally very similar system that, in contrast to the complex reported here, shows single molecule magnetic properties, and this is in agreement with the quantum-chemical prediction and analysis.

Introduction

Single-molecule magnetism (SMM) is a quantum phenomenon of fundamental importance with a range of possible applications.[1–5] Barriers of magnetization relaxation between the two degenerate ground states of opposite electron spin of over 1000 cm^{-1} (1440 K) have been reported but fast relaxation, also including tunneling processes, still prevent many putative applications such as data storage, quantum computing and spintronics.[6–8] Key features in the endeavor to improve the SMM performance are increasing the effective anisotropy barrier and suppression of quantum tunneling.[9–13] After a decade of searching for maximum spin multiplicities, with molecules of total spin up to $S=83/2$ (e.g., a ferromagnetically coupled Mn$^{III}_{12}$Mn$^{II}_7$ cluster),[14,15] efforts in the last decade concentrated on maximizing the magnetic anisotropy, and heavy transition metal ions and lanthanides with large spin-orbit coupling have come into focus.[16,17]

While there are various attempts for the "rational design" of SMMs,[10] the optimization in terms of increased effective barriers U_{eff} for magnetization relaxation has not been as efficient as one might have hoped (record effective barriers of magnetization relaxation that have been observed with various types of SMM architectures are 652 cm^{-1} for a mononuclear Tb^{III} compound with phthalocyanine ligands,[7,8] 1,541 cm^{-1} for a dysprosocenium complex,[18–20] and 242 cm^{-1} for a nitrogen-radical-bridged bis-terbium(III) species.[21]) Possible reasons are that the efficient and accurate theoretical description of the magnetic anisotropy,[13,22–25] and its dependence from structure (magneto-structural correlations) have only recently started to become available,[26,27] and the prediction and enforcement of coordination geometries of lanthanides are much less developed than that of transition metal ions.[11,12,28]

[a] Prof. Dr. P. Comba, Prof. Dr. M. Enders, Dr. M. Großhauser, Dr. M. Hiller, Dr. D. Müller, Prof. Dr. H. Wadepohl
Universität Heidelberg
Anorganisch-Chemisches Institut INF 270
69120 Heidelberg (Germany)
E-mail: peter.comba@aci.uni-heidelberg.de

[b] Prof. Dr. P. Comba, Dr. D. Müller
Interdisziplinäres Zentrum für Wissenschaftliches Rechnen, IWR
Universität Heidelberg INF 270
69120 Heidelberg (Germany)

[c] Prof. Dr. R. Klingeler, Dr. C. Koo, M. Tavhelidse
Kirchhoff-Institut für Physik
Universität Heidelberg, INF 227
69120 Heidelberg (Germany)
E-mail: klingeler@kip.uni-heidelberg.de

[d] Prof. Dr. R. Klingeler
Centre for Advanced Materials (CAM), INF 225
69120 Heidelberg (Germany)

[e] Prof. Dr. G. Rajaraman, A. Swain
Department of Chemistry
Indian Institute of Technology Bombay
Powai, Mumbai 400076 (India)

Chemistry–A European Journal

Full Paper
doi.org/10.1002/chem.202100626

Chemistry Europe
European Chemical
Societies Publishing

Here, we adopt a well-established computational scheme to determine the electronic ground state, magnetic exchange and relaxation pathways, based on an ab initio CASSCF wavefunction, spin-orbit coupling via the restricted active space state interaction method, followed by an analysis of the multiplet splitting derived from the Lines model and a ligand field analysis involving extended Stevens operators.[29–31] Although this procedure has been used extensively and successfully, in particular for oligonuclear 4f and mixed 3d–4f systems,[17] it is not undisputed[24] and has only recently started to be rigorously validated with the comparison of computed with experimentally determined spectroscopic parameters in addition to SQUID data (χT vs. T) which, admittedly, are not very sensitive. In studies related to the present publication, we have reported homodinuclear lanthanide(III) and heterodinuclear 3d–4f systems, where the computational data were validated with a combination of AC and DC SQUID, high-frequency/high-field EPR (HF-EPR) and MCD data, combined with an extensive ligand field analysis based on angular overlap model (AOM) calculations,[32,33] and similar approaches have also been used successfully in the validation of the computed multiplet splitting and relaxation barriers in combination with the respective experimental data of mononuclear dysprosium(III) complexes.[34,35] We now extend this validation with the experimental evaluation of the magnetic anisotropy by paramagnetic NMR spectroscopy as well as single crystal AC SQUID and HF-EPR experiments of the $[Dy^{III}\{Ni^{II}(L)\}_2]ClO_4$ complex shown in Scheme 1; the structure, magnetism and NMR data of the entire series of $[Ln^{III}\{Ni^{II}(L)\}_2]^+$ complexes with Ln=Y, La, Ce, Nd, Sm, Eu, Gd, Tb, Dy, Ho, Er, Tm, Lu was already reported.[36] Note that there are two crystal structures of $[Dy^{III}\{Ni^{II}(L)\}_2]^+$ with slightly different structural parameters, $[Dy^{III}\{Ni^{II}(L)\}_2]ClO_4$ vs. $[Dy^{III}\{Ni^{II}(L)\}_2]ClO_4 \cdot MeOH$ (see also Supporting Information, Tables S6, S7).[36] The experimental single crystal SQUID and HF-

EPR data reported here are from the MeOH-free crystals while the earlier reported powder SQUID data refer to the structure with a MeOH of crystallization. The computational work discussed here in detail therefore is based on the MeOH-free structure, computational data involving the other structure (see Supporting Information, Tables S1-S4) indicate that the electronic and magnetic properties of the second structure are, as expected, slightly different but the SMM properties differ only marginally and this is therefore not discussed here in detail.

Results and Discussion

Ab Initio Quantum Chemical Analysis

The heterotrinuclear $Ni^{II}_2Dy^{III}$ complex was studied in detail with ab initio quantum chemical methods using Molcas 8.0.[37] The local magnetic and electronic properties were determined within an established fragmented approach on the crystal structural coordinates, where the neighboring magnetic centers are substituted with their closest diamagnetic analogue, i.e., Dy^{III} was substituted by Lu^{III}, and Ni^{II} by Zn^{II}.[23] All atoms were described by contracted ANO-RCC basis sets with one additional polarization function.[38,39] The CAS(8,5) wavefunction for Ni^{II} accounts for the required spectroscopic terms ^1S, ^1D, ^1G, ^3P and ^3F, and the corresponding states are mixed with the RASSI module, which also contributes the spin-orbit coupling effects (see Table S2).[29] The triplet ground state of the Ni^{II} ions is well reproduced, with nearly isotropic g tensors ($g_x=g_y\approx g_z$) and a very small axial zero-field splitting of $D\approx+2.5$ cm^{-1} (see Table 1). The coupling of the 21 sextet terms of the CAS(9,7) wavefunction of Dy^{III} leads to eight Kramers doublets of the $^6H_{15/2}$ ground state (see Table 2). As noted before, there are two slightly different crystal structures of $[Dy^{III}\{Ni^{II}(L)\}_2]ClO_4$. Since the single crystal SQUID and HF-EPR experiments were done on the structure of the MeOH-free crystals, the computational data reported here (specifically in Tables 1, 2) are based on the experimental coordinates of that structure – computational data from the other structure are only slightly different and appear in the Supporting Information (Tables S2-S6).

For the Dy^{III} center the computational results yield a feebly axial ground-state with small energy separations of the respective Kramers doublets. These also show various orientations of their magnetic moments (as shown in the last column of Table 2, indicating the deviation of the magnetic axis with respect to the ground-state KD1). These features lead to a fast
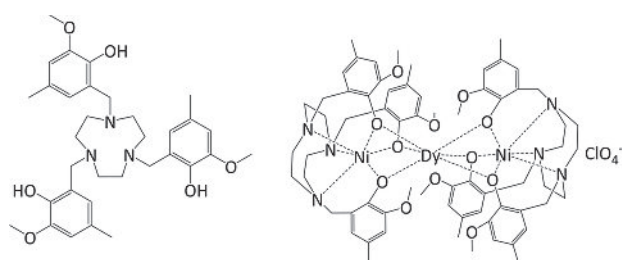
Scheme 1. Chemical structure of H₃L and the heterotrinuclear $[Dy^{III}\{Ni^{II}(L)\}_2]$ ClO₄ complex.

Table 1. Electronic properties of the $[(Lu)\{(Ni)(Zn)(L)_2\}]^+$ fragments. All states of the spectroscopic manifold are considered for the RASSI-SO coupled CAS (8,5) wavefunction. g tensor components and anisotropy parameters are calculated for the triplet ground-state within the SINGLE_ANISO module.

state	RASSI energies [cm^{-1}]		g Tensors and anisotropy parameters		
	Ni1	Ni2		Ni1	Ni2
1	0.00	0.00	g_X	2.27	2.27
2	2.83	2.67	g_Y	2.27	2.27
3	3.69	2.81	g_Z	2.24	2.25
4	8348.73	8235.99	D [cm^{-1}]	2.54	2.43
5	8466.69	8303.69	E [cm^{-1}]	-0.74	−0.05
6	8525.88	8380.72			

Table 2. Electronic properties of the $[(Dy)\{(Zn)_2(L)_2\}]^+$ fragment. All 21 sextet states of the spectroscopic manifold are considered for the RASSI-SO coupled CAS(9,7) wavefunction. g tensor components and anisotropy parameters are calculated for the Kramers doublets of the $^6H_{15/2}$ ground-state within the SINGLE_ANISO module.

Kramers doublet	RASSI energies [cm^{-1}]	g_x	g_y	g_z	⊳ KD1-Dy-KDX [°]
1	0.00	0.13	0.52	14.95	–
2	36.38	0.00	0.36	15.41	19.8
3	62.19	0.04	0.42	12.91	36.8
4	180.18	3.32	3.76	9.15	13.7
5	208.38	0.13	0.16	19.66	22.4
6	332.35	5.72	5.53	1.61	96.6
7	458.75	4.33	3.72	0.22	94.0
8	534.56	12.19	8.67	1.15	19.5

relaxation of magnetization,[34,40,41] which is confirmed by experiments where no stabilization of the magnetization is observed. The feeble axiality is a result of the ligand field. Even though the symmetry with a distorted trigonal prism around the Dy^{III} center seems reasonably appropriate, the six oxygen donors are not enough to satisfy the demanding coordination sphere of a Dy^{III}. Table S1 lists the extended Stevens Parameters B^q_k in the coordinate system of the magnetic axis of the ground state Kramers doublet (see Figure 1). The negative sign of B^0_2 indicates the general axiality of the system but the large value of B^1_2 is the result of a relatively large component in the xz plane. This rhombic component is probably the result of the phenolate-oxygen O5 and its neighboring methoxy group, which are in the xz plane of the parametrization. An analysis of the m_J coefficients of the RASSI wavefunction gives insight into the shape of the ground state KD1. The total coefficients are $0.64|\pm13/2> + 0.31|\pm9/2> + 0.26|\pm15/2> + 0.24|\pm11/2>$. The lack of stabilization of the desired $|\pm15/2> m_J$ state is a result of the weak axial ligand field around Dy^{III} and therefore leads to a small overall contribution to the ground state KD1.[16]

It is common practice to determine magnetic properties of lanthanide(III) ions in a smaller pseudo-spin basis. This is a reasonable approach for a comparison with experiments at low temperature. However, for the validation of our computational approach, we also use the analysis of paramagnetic NMR experiments at a temperature of 340 K,[36] where one has to account for the population of the entire $^6H_{15/2}$ ground state multiplet and not only the lowest Kramers doublet. The

Hamiltonian for the corresponding $[(Dy)\{(Zn)_2(L)_2\}]^+$ fragment (see Table 2) is set up in the basis of the 16 functions of the ground state multiplet, which results in an axial parameter $D = -6.7$ cm^{-1} and a rhombic contribution $E = 0.45$ cm^{-1} [Eq. (1)], where D and E correspond to axial and rhombic ligand field parameters. The value of the axial parameter D is in reasonably good agreement with the susceptibility tensor parameters χ obtained by NMR spectroscopy (see below; Eq. (2) allows[42,43] to approx. convert the susceptibility tensor parameter $\Delta\chi_{ax}$ to D): with $g_J = 4/3$, $J = 15/2$ and $\Delta\chi_{ax} = 4.566 \cdot 10^{-31}$ m^3 (see below), $D^{NMR} = -5.0$ cm^{-1} (vs. $D^{QM} = -6.7$ cm^{-1}) results.

$$\widehat{H}_{ZFS} = D\left(S_z^2 - \frac{S(S+1)}{3}\right) + E(S_x^2 - S_y^2) \tag{1}$$

$$D = \left(\frac{-30\,k^2\,T^2\Delta\chi_{ax}}{\mu_0\mu_B^2 g_J^2 J(J+1)(2J-1)(2J+3)}\right) \tag{2}$$

The DC SQUID data can be used to quantify the exchange coupling between the different metal ions in the Lines model approach.[30,44–46] In this approach, the *ab initio* computed single ion anisotropies of the Ni^{II} centers, the g anisotropy, and the corresponding energies of Dy^{III} center are taken into consideration. The only unknown parameters for obtaining the susceptibility are the magnetic exchange interactions J_{NiDy}, J_{NiNi} and a possible intermolecular interaction zJ between the trinuclear subunits in the solid. However, while the usual DFT-based broken-symmetry approach[47] generally yields predictions of appreciable accuracy,[48–50] the relatively weak coupling does not allow to compute an accurate enough set of parameters, and the feeble dependence of the DC SQUID data from the exchange coupling does not allow an accurate enough validation (see Supporting Information). Therefore, the J values used here are those resulting from the HF-EPR measurements (see below).
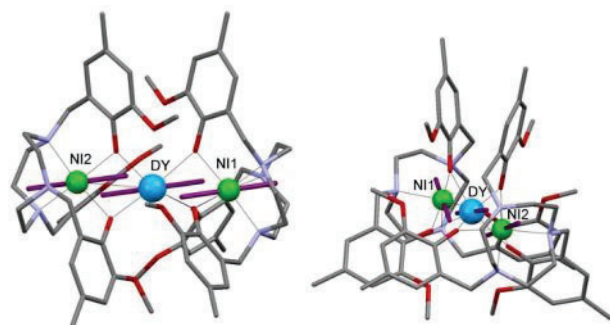

Figure 1. Plot of two orientations of the trinuclear complex with the ab initio calculated orientations of the anisotropies of the three metal ions in the ground state.

Paramagnetic NMR Spectroscopy

^{1}H and ^{13}C{^{1}H} NMR spectra of $[Dy^{III}\{Ni^{II}(L)\}_2]^+$ in 1,2-C$_6$D$_4$Cl$_2$ were recorded at 340 K, and the assignment of the observed signals has been described in detail.[36] The corresponding χ tensor can be fitted from the chemical shifts together with the structural data obtained from the X-ray structural analysis. This was found

Chemistry–A European Journal

Full Paper
doi.org/10.1002/chem.202100626

Chemistry Europe
European Chemical
Societies Publishing

to be primarily axial with an axial anisotropy of $\Delta\chi_{ax} = 4.6 \pm 0.1 \cdot 10^{-31}$ m^3. This value was found to correspond well to that predicted by an electrostatic point charge model ($4.2 \cdot 10^{-31}$ m^3 for 298 K).[51] There are several approaches to estimate the susceptibility anisotropies from crystal field effects. The most commonly used is that proposed by Bleaney, which is based on the assumption that the ligand field splitting of the M_J levels is small compared to the thermal energy at ambient temperature. This is reflected in the approximation that all M_J levels are equally populated. The corresponding equation for the axial part of the pseudo-contact shift then retains only the B_2^0 crystal field parameter, while higher order terms vanish. This results in Equation (3) for the calculation of $\Delta\chi_{ax}$.

$$\Delta\chi_{ax} = -\frac{\mu_0\mu_B^2 g_J^2 J(J+1)(2J-1)(2J+3)}{10k^2T^2} \cdot \langle J\|\alpha\|J\rangle \cdot B_2^0 \qquad (3)$$

In order to use Equation (3) the B_2^0 crystal field parameter has to be known and for the comparison presented here, its value was derived from the results of the quantum chemical analysis, and this has been shown to generally lead to very accurate predictions.[34] The equation is obtained considering only the T^{-2} dependence of the pseudo-contact shift. It has been argued that this simplification may be unjustified and an approach to include the T^{-3} term was presented.[52] The corresponding formula then contains contributions from higher order crystal field parameters. An equation was also developed that allows the numerical calculation of the χ tensor components, from which the $\Delta\chi_{ax}$ value can be obtained [Eq. (4)]:[53]

$$\chi_{\alpha\beta} = \frac{1}{\sum_i e^{-E_i/kT}} \cdot$$
$$\sum_i \left\{ \left[\sum_j \frac{\frac{\langle i|\mu_\alpha|j\rangle\langle j|\mu_\beta|i\rangle}{kT} -}{\sum_j \frac{\langle i|\mu_\alpha|j\rangle\langle j|\mu_\beta|i\rangle + \langle i|\mu_\beta|j\rangle\langle j|\mu_\alpha|i\rangle}{E_i - E_j}} \right] \cdot e^{-E_i/kT} \right\} \qquad (4)$$

The contributions of the individual M_J states to the eigenfunctions have to be known, as well as their respective energy eigenvalues. These have been taken from the quantum chemical analysis. The calculation of the χ tensor has been accomplished using a custom-written script for Octave 4.0. Details of the calculations are given as Supporting Information. The calculated values for $\Delta\chi_{ax}$ and $\Delta\chi_{rh}$ using Equation (3) and S5, respectively (see Supporting Information) and the numeric calculation [Eq. (4)] are summarized in Table 3.

From the values it emerges that the Bleaney approach [Eq. (3)] reproduces the sign of the axial susceptibility anisotropy correctly but the agreement of the values is not

particularly good. Especially the rhombic component is larger than that obtained experimentally. In contrast, the numerical calculation gives far better agreement for both the axial and rhombic components. This is of importance, as it demonstrates that the Stevens parameters obtained from the ab initio quantum-chemical calculations accurately reproduce the experimental observations (see Supporting Information). Note that the principal directions of the fitted and calculated tensors do not coincide precisely, and this may lead to some inaccuracies. Importantly, the experimental susceptibility parameters are also in good agreement with the predictions based on the ab initio quantum-chemical calculations. This follows from the conversion of the experimental susceptibility anisotropies $\Delta\chi_{ax}$ to the computed axial anisotropies D (see above); note however that this comparison involves the Bleaney approach which has been shown to be slightly less accurate than the numerical approach (see Table 3).

Static Magnetic Susceptibility and Magnetization of Single Crystals

The static magnetic susceptibility $\chi = M/B$ has been measured on single crystals along the different crystallographic axes. Note that there are two slightly different structures.[36] That of the crystals used for the single crystal magnetic and HF-EPR measurements is the methanol-free one. The crystal structure has two differently oriented molecules as sketched in Figure 2 that shows the orientation of the trinuclear complexes in the unit cell (the detailed structure is shown in Figure 1).

The product of static magnetic susceptibility and temperature, $\chi_{mol}T$, in the temperature range T = 2–300 K is shown in Figure 3a. The measurements have been performed at $B = 0.5$ T applied along the three crystalline axes, respectively. For all three orientations, $\chi_{mol}T$ shows constant values above 150 K, i.e., 12.9(6) erg K/G^2 mol for the a axis, 15.6(8) erg K/G^2 mol for the b axis, and 17.3(9) erg K/G^2 mol for the c axis, at 300 K each. The theoretical $\chi_{mol}T$ value at T = 300 K in consideration of $J_{Dy} = 15/2$, $g_{Dy} = 4/3$ for the Dy^{III} ion and $S_{Ni} = 1$, $g_{Ni} = 2.14$ for the two
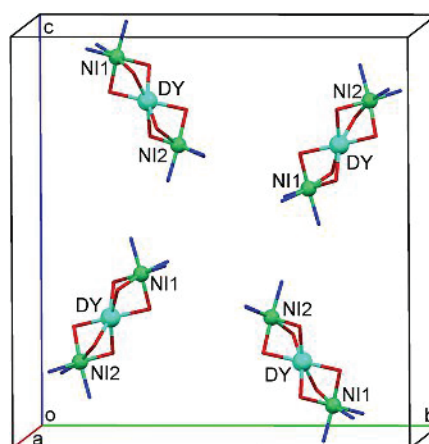
Table 3. Comparison of experimental and calculated susceptibility anisotropies.

	$\Delta\chi_{ax}$ (10^{-31} m^3)	$\Delta\chi_{rh}$ (10^{-31} m^3)
experimental	4.6 ± 0.1	0.2 ± 0.1
Eq. (3) and (S5)	3.1	0.8
Eq. (4)	4.1	0.3

Figure 2. Orientation of the molecules in the unit cell of [Dy^{III}{Ni^{II}(L)}$_2$]ClO$_4$.

Chemistry–A European Journal

Full Paper
doi.org/10.1002/chem.202100626

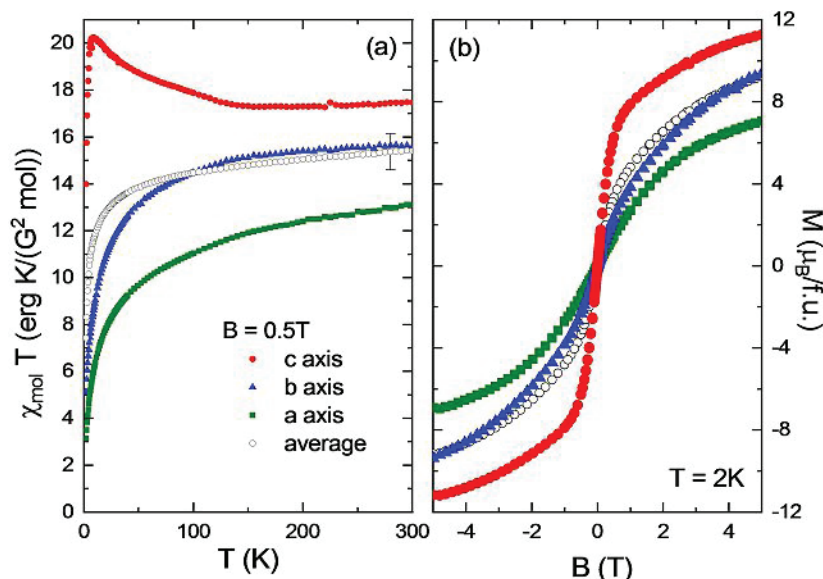**Chemistry
Europe**
European Chemical
Societies Publishing

Figure 3. a) Temperature dependence of $\chi_{mol}T$ *vs.* T along the three crystallographic axes at $B = 0.5$ T (colored) and its average (black). (b) Field dependence of the magnetization along the three crystal axes and its average, at $T = 2$ K.

Ni^{II} ions is 16.47 erg K/G^2 mol, which is reasonably close to the average of the three orientations of $\chi_{mol}T = 15.4(8)$ erg K/G^2 mol. Upon cooling below 100 K, $\chi_{mol}T$ for the *a* and the *b* axis decreases while it displays an upturn behavior with a maximum at $T_{max} \approx 8$ K for $B||c$. Below T_{max}, the susceptibility also rapidly drops for $B||c$, implying magnetic anisotropy or antiferromagnetic interaction in the complex. From the distinct $\chi_{mol}T$ behavior, the easy axis of the $[Dy^{III}\{Ni^{II}(L)\}_2]ClO_4$ single crystal is along or at least in the close vicinity of the crystallographic *c* axis. As will be shown from the analysis of the HF-EPR data, the easy axis does not perfectly match the *c* axis.

The magnetization curves at $T = 2$ K for the three crystalline axes of the single crystal confirm the pronounced magnetic anisotropy at low temperature (Figure 3b). While the *M vs. B* data for the *a* and *b* axes exhibit a smooth right-bending without a tendency to saturation in the experimentally accessible magnetic field range, the data for the *c* axis displays a much steeper initial slope and a slight kink at around $B \approx 0.5$ T, which reminds on a ferromagnetic-like behavior. Here, the magnetization at $B = 5$ T amounts to $M_S = 11.3(6)$ μ_B/f.u.. No hysteresis is observed in the magnetization data at 2 K for any orientation.

High-Frequency/high-Field EPR Spectroscopy

HF-EPR measurements were carried out along the *c* and *b* axis of the $[Dy^{III}\{Ni^{II}(L)\}_2]ClO_4$ single crystal. The EPR spectra for the magnetic field applied along the *c* axis at fixed frequency of f = 131.7 GHz and at various temperatures are shown in Figure 4a. At $T = 2$ K, four distinct resonances are observed in the spectra, and they are labeled with symbols as shown in the figure. As temperature increases from 2 K, all resonance features become less pronounced and finally disappear at slightly different

temperatures, *i.e.*, the triangle resonance disappears at $T = 8$ K, the square one at 10 K, and the circle one at 13 K. As the temperature dependencies reflect the Boltzmann distribution of spins in the associated spin states this behavior implies that the three resonances reflect transition between the spin ground state which is identical in all three cases and different final states (see the energy level diagram in Figure S2). The resonance with strongest intensity, *i.e.*, the one marked by the circle, is associated with the transition between the spin ground state and the lowest excited state. The fourth resonance feature marked by the down triangle, however, shows a different temperature dependence. As temperature increases, its intensity slightly decreases and then increases, which indicates that the initial state of the transition is not the spin ground state but an excited state. Note, that the additional feature between the inverse triangle and circle resonances and the wiggles at $B > 4.5$ T display similar temperature dependencies as the down triangle one. This implies that all these features are assigned as the excited state resonance.

The frequency dependence of the four distinct resonance fields labelled in Figure 4a, at $T = 2.2$ K, is shown Figure 4b. The spectra obtained at various fixed frequencies between 89.1 and 430.8 GHz are shown in the Supporting Information (Figure S3). The four resonance branches are non-equally separated and exhibit a linear behavior at high fields, which provides the effective *g* factors. All resonance modes except the triangle resonance have $g_c = 2.13(1)$. The slope of the triangle resonance branch is about two times larger, *i.e.* $g \approx 4$, indicating a forbidden transition. At low magnetic field, bending of the resonance branches indicates mixing of the associated spin states while at $B = 0$ T there is finite zero-field splitting (ZFS).

In order to explain the observed data, the resonance branches are simulated by means of the matrix diagonalization of an appropriate Hamiltonian. Here, it is worth to review the
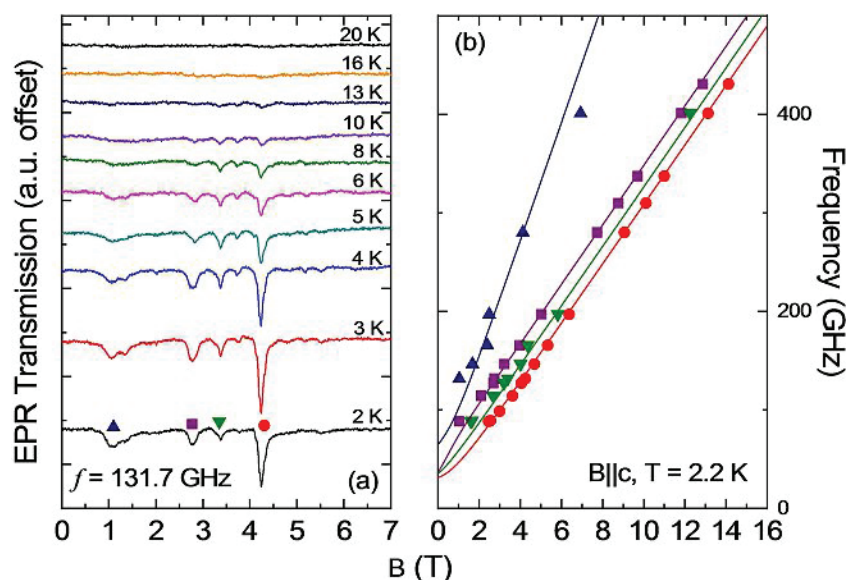
Chemistry–A European Journal

Full Paper
doi.org/10.1002/chem.202100626

Chemistry Europe
European Chemical
Societies Publishing

Figure 4. (a) Temperature dependence of the HF-EPR spectra in the temperature range 2 K to 20 K, at $f = 131.7$ GHz and $B||c$-axis. (b) Frequency-magnetic field diagram of the resonance fields at $T = 2.2$ K and $B||c$. Data symbols correspond to the resonances in the spectra in (a), respectively. Solid lines represent simulations according to Equation (5) (see the text).

molecular structure and coordinates of the magnetic ions in $[Dy^{III}\{Ni^{II}(L)\}_2]^+$, since the EPR data are affected by these factors. In $[Dy^{III}\{Ni^{II}(L)\}_2]^+$, the three magnetic ions are almost linearly arranged (see Figure 2) with a Ni–Dy-Ni bonding angle of 177.8°. The NiO_3N_3 octahedra and the DyO_6 polyhedron are linked through six oxygen ions. According to the quantum chemical calculations, one of the Ni moments and the Dy moment have collinear magnetic axes while the other Ni moment is tilted by 36° from these (see Figure 1). In the single crystal, two differently oriented molecules are found, which are misaligned by 65.3° and twisted by 31° to each other (see Figure 2). Along the c and b axes, however, these two molecules are symmetrical.

Due to the strong axial anisotropy of the Dy moments, the Ising concept[54] is applied to simulate the spectra by means of an appropriate Hamiltonian, i.e.,

$$\widehat{H} = -J_{Dy-Ni}\left(\vec{\widehat{J}}_{Dy} \cdot \vec{\widehat{S}}_{Ni_1} + \vec{\widehat{J}}_{Dy} \cdot \vec{\widehat{S}}_{Ni_2}\right)$$
$$-J_{Ni-Ni}\widehat{S}_{Ni_1} \cdot \widehat{S}_{Ni_2} + \sum_i^2 \widehat{S}_{Ni_i} \cdot \vec{\widehat{R}}_i^T \cdot \vec{\widehat{D}}_i \cdot \vec{\widehat{R}}_i \cdot$$
$$\widehat{S}_{Ni_i} + \mu_B\widehat{B}^z\left(g_{Dy}\vec{\widehat{J}}_{Dy}\right) + \sum_i^2 \mu_B\widehat{B} \cdot \vec{\widehat{R}}_i^T$$
$$\cdot\vec{g}_{Ni_i} \cdot \vec{\widehat{R}}_i \cdot \widehat{S}_{Ni_i}$$

(5)

The first and second terms describe the exchange interaction between the Ni and Dy moments and between the Ni moments by means of the exchange coupling parameters J_{Dy-Ni} and J_{Ni-Ni}, respectively. The third term accounts for the magnetic anisotropy of the Ni spins. The misaligned magnetic axes are considered through the rotational matrix $\vec{R}$ by the Euler angle.

The tensor operator $\vec{D}$ can be written using an axial anisotropy term D_{Ni}, and a transversal one E_{Ni}, in the spin eigenstate frame. The fourth and fifth terms are the Zeeman terms for the Dy and the two Ni moments, respectively. In the latter term, the rotational matrix is again applied to the g tensor of Ni. Note, that due to the abovementioned symmetry of the local magnetic axes of the Ni ions (see Figure 1) the analysis in terms of Equation (5) will yield a single g_c value for both Ni ions. Following the Ising concept, only the z component of the Dy magnetic moment is considered.

Applying the Hamiltonian of Equation (5) to the experimental data allows to simulate the magnetic resonance branches in Figure 4b. For the simulations, the abovementioned characteristics of each branch inferred from the experimental data at various temperatures and the molecular structure of the complex have been used as constraints. The spin of the Ni ions and the size of the Ising spin of the Dy ion have been fixed as $S_{Ni}=1$, $J_{Dy}=15/2$, and $g_{Dy}=4/3$, respectively. The best simulations of the experimental resonance modes are shown in Figure 4b as solid lines. The corresponding parameters are $g_{Ni, c\text{-axis}}=2.16(2)$, $D_{Ni}=-1.5(2)$ cm^{-1}, $E_{Ni}=0.5(1)$ cm^{-1}, $J_{Dy\text{-}Ni}=0.05(2)$ cm^{-1}, and $J_{Ni\text{-}Ni}=0.03(4)$ cm^{-1}. The g value is reasonably close to the typical g factor of Ni ions in distorted octahedral environment.[55] We emphasize that our analysis implies that the crystallographic c axis is close to an effective overall easy axis of the crystal but slight bending of the branches at low magnetic field implies that the c axis does not perfectly match the easy axis situation. The fact that two subsets of resonance branches associated with the two orientations of molecules in the single crystalline matrix are not observed is consistent with the assumption that the anisotropy axes of the molecules are rather symmetric with respect to the measurement axes (see Figures 1, 2).

Chemistry–A European Journal

Full Paper
doi.org/10.1002/chem.202100626

Chemistry Europe
European Chemical
Societies Publishing

The magnetic anisotropy and the molecular structure attribute to the different EPR branches when the magnetic field is applied in different orientations. Figure 5 shows the EPR spectra with the magnetic field applied along the b axis of the single crystalline sample. For $B||b$, only three resonance features are observed in contrast to the findings for $B||c$ displayed in Figure 4. From the temperature dependence of the peak intensities and a steeper slope, $g \approx 4$, of the resonance branch in the frequency-field diagram, the triangle resonance is assigned as a forbidden transition. Due to the relatively strong peak intensity, the circle resonance can be assigned as the ground state resonance. The down triangle resonance vanishes at low temperatures as shown in Figure 5a, implying that the final state of the resonance is a higher excited state than in the case of the circle resonance. The estimated g factor for the circle and down triangle resonance modes is $g_b = 2.14(1)$.

The observed resonance branches for $B||b$ (Figure 5b) are again simulated with the Hamiltonian of Equation (5) as for $B||c$. For the best simulation, the same parameters were used as for $B||c$, except for a slightly different g value of the Ni ions, i.e., $g_{Ni, \text{b-axis}} = 2.17(2)$. When determining these parameters, we have focused on the matching of the ground state and the forbidden resonance branches because both are related to the ground state. In contrast, the simulated excited state resonance mode does not match the experimental data very well but only shows qualitative agreement.

General Discussion of the Experimental and Computational Parameters

The HF-EPR data are well described by the Hamiltonian of Equation (5) and the parameters listed above. The appearance of the ZFS clearly confirms magnetic anisotropy, which is also seen in the static magnetization data, where the c axis magnetization by far exceeds the magnetization along the other crystallographic directions. Indeed, the analysis of the HF-EPR data implies a negative D value for the Ni^{II} ions, i.e. $D_{Ni} = -1.5(2)$ cm^{-1}, which indicates axial anisotropy of the Ni^{II} ions. For an individual molecule, despite misalignment of the magnetic axes of the two Ni ions with respect to each other, the parallel alignment of one of the Ni moments with the Dy^{III} one attributes to the dominant axial-type anisotropy of the complex. Note again that due to the strong magnetic anisotropy of the Dy^{III} ion, the Ising spin concept is applied for the analysis of the HF-EPR data.

Despite the fact that the crystal structure exhibits two differently oriented molecules, which usually results in two magnetic anisotropy axes and hence two sets of EPR resonance features,[56] only one set of branches is observed in the experimental data. Only in some spectra obtained for $B||b$ at high frequency, e.g., at f = 260 and 392.6 GHz, a double feature of the ground state resonance is resolved (see Supporting Information, Figure S4, resonances marked by red circles). Coincidently in the given complex, the two molecules are symmetric along the c and b axes of the crystal, leading to the observed single set of resonance features. The observed double feature at high frequency may result from a small misalignment of the crystal due to imperfect mounting.

In addition to axial anisotropy, a strong transverse anisotropy is also present in $[Dy^{III}\{Ni^{II}(L)\}_2]ClO_4$. From the simulation of the EPR data, we obtain an E_{Ni} value that is close to its maximum value given by $E/D = 1/3$. Due to the large rhombicity with $E/D = 0.3$, the spin states are strongly mixed. Experimentally, large rhombicity and hence significant mixing of the states is confirmed by the clear observation of the forbidden resonance branch associated with spin state transitions $\Delta S_z > \pm 1$, which is observed as a strong feature in the spectra for both
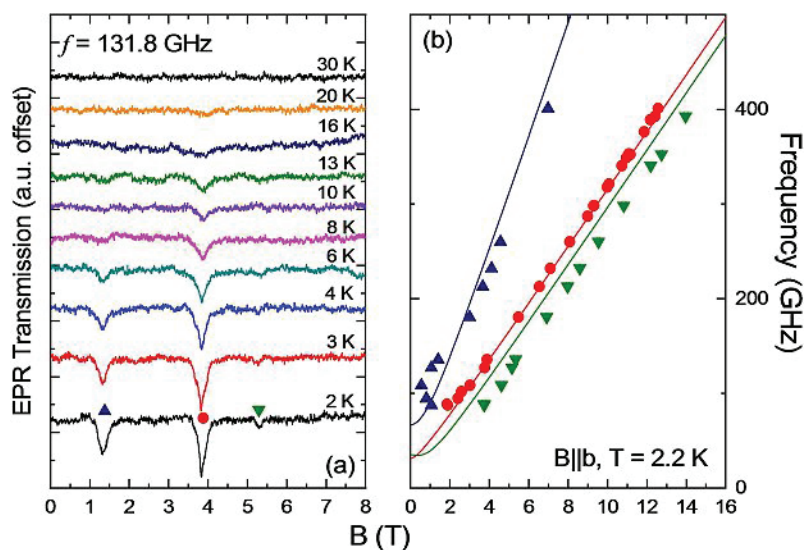

Figure 5. (a) Temperature dependence of HF-EPR spectra in the temperature range 2 to 30 K, at f = 131.6 GHz and $B||b$ axis. (b) Frequencies-magnetic field diagram of the resonance fields at T = 2.2 K and $B||b$. Data symbols correspond to the resonances in the spectra in (a), respectively. Solid lines represent fits according to Equation (5) (see the text).

Chemistry–A European Journal

Full Paper
doi.org/10.1002/chem.202100626

Chemistry Europe
European Chemical
Societies Publishing

field orientations. In contrast to the obtained anisotropy parameters, the magnetic exchange interaction $J_{Dy-Ni} = 0.05(2)$ cm^{-1}, and $J_{Ni-Ni} = 0.03(4)$ cm^{-1} is less precisely determined by the HF-EPR data because in our simulation the exchange interaction is a rather loose constraint and its error is quite large. Unfortunately, the SQUID data in combination with the quantum-chemical calculations do also not allow for an accurate determination of the exchange coupling constants (see above and Supporting Information, Figure S1). However, the EPR data clearly imply that finite ferromagnetic exchange has to be included to simulate the resonance branches appropriately. Moreover, the exchange interaction must be small as compared to the magnetic anisotropy, i.e., $J \ll D$, resulting in small energy differences between the ground state and the excited states. This interpretation is in agreement with experimental observations of published oligonuclear Ni^{II}Dy^{III} species with phenolate bridges, where small ferromagnetic exchange between the metal centers and $J \ll D$ was reported.[57,58] Indeed, there is further evidence of finite magnetic interaction in the spectra because additional resonance features, e.g., wiggles in Figure 4, are observed. Their temperature dependence is different from the ground state resonance, which supports the assignment to the excited states and thus the presence of finite exchange interaction. Finally, we note that the g value of the Ni^{II} ions is almost isotropic, which is typical for Ni^{II} ions in a distorted octahedral environment.[43]

Comparison of [Dy^{III}{Ni^{II}(L)}$_2$]$^+$ with a Structurally Similar [Dy^{III}{Ni^{II}(L')}$_2$]$^+$ System

Recently, a trinuclear [Dy^{III}{Ni^{II}(L')}$_2$]$^+$ complex with a very similar overall structure to that of [Dy^{III}{Ni^{II}(L)}$_2$]$^+$ described here was reported (see Figure 6 for a visualization of the similarities of the two structures).[59] Interestingly, in contrast to our [Dy^{III} {Ni^{II}(L)}$_2$]$^+$ complex, [Dy^{III}{Ni^{II}(L')}$_2$]$^+$ shows SMM behavior. We therefore analyze reasons for this interesting discrepancy. Structurally, the two systems are very similar, with two terminal trigonal Ni^{II} sites (pseudo-octahedral) capping a hexacoordinate trigonal Dy^{III} center (pseudo-octahedral with a twist towards trigonal prismatic). We anticipate that the ligand field exerted by the three imine nitrogen donors in [Dy^{III}{Ni^{II}(L')}$_2$]$^+$ with respect to the three tertiary amines in [Dy^{III}{Ni^{II}(L)}$_2$]$^+$ do not alter the ligand field substantially.[60–62] The shape analysis of the two Ni^{II} and the Dy^{III} centers for both complexes indicates that the main structural difference is around the Dy^{III} center, which seems to have somewhat more trigonal prismatic character for [Dy^{III}{Ni^{II}(L')}$_2$]$^+$ but the difference is relatively small (see Table S8).[63] It seems, however, that the shape analysis does not lead to an appropriate description of the ligand field symmetry, and we have therefore also measured the trigonal twist angles ϕ (60° and 0° for an octahedron and a trigonal prism, respectively) and the elongation of the coordination polyhedra along the trigonal axes.[64] The average trigonal twists of the two Ni^{II} centers are $\phi = 50$° for both, [Dy^{III}{Ni^{II}(L)}$_2$]$^+$ and [Dy^{III} {Ni^{II}(L')}$_2$]$^+$, i.e. all Ni^{II} centers are moderately trigonally distorted octahedral, and the distances between the two trigonal planes each, defined by the three N (amine or imine) donors and the three phenolate oxygen donors, respectively, are 2.64 Å for [Dy^{III} {Ni^{II}(L)}$_2$]$^+$ and 2.51 Å for [Dy^{III}{Ni^{II}(L')}$_2$]$^+$, i.e. the latter structure is slightly more compressed along the trigonal axis, and this results primarily from significantly more acute angles in the trigonal N$_3$ caps of the triazacyclononane groups of the Ni^{II} center of [Dy^{III}{Ni^{II}(L)}$_2$]$^+$ (approx. 86° vs. 96° for [Dy^{III}{Ni^{II}(L)}$_2$]$^+$ and [Dy^{III}{Ni^{II}(L')}$_2$]$^+$, respectively). However, these are relatively small differences, and in both complexes the Ni^{II} centers are quite similar, slightly trigonally distorted octahedral with the expected metal-donor distances, and the ligand field around
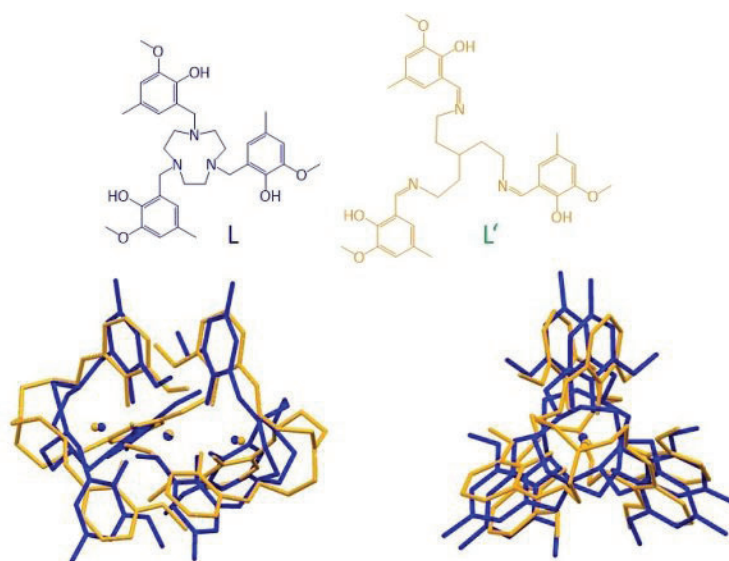

Figure 6. Comparison of [(Dy){(Ni)$_2$(L)$_2$}]$^+$ (blue) and [(Dy){(Ni)$_2$(L')$_2$}]$^+$ (orange). a) structural schematic of the ligands, b) overlay of the solid state structures, superimposed to give the smallest RMS deviations for the metal and oxygen donor atoms (data for the experimental structures have been published[36,59]).

Chemistry–A European Journal

Full Paper
doi.org/10.1002/chem.202100626

Chemistry Europe
European Chemical
Societies Publishing

the Ni^{II} centers is not expected to change significantly. The structural analysis shows, however, that there are significant structural differences around the Dy^{III} centers: the trigonal twist analysis indicates that in [Dy^{III}{Ni^{II}(L)}$_2$]$^+$ the Dy^{III} center is half way between octahedral and trigonal prismatic, while for [Dy^{III}{Ni^{II}(L')}$_2$]$^+$, the structure is closer to octahedral ($\phi = 31°$ vs. $\phi = 48°$), and the distances between the trigonal planes are also rather different, i.e. 3.29 Å vs. 3.67 Å for [Dy^{III}{Ni^{II}(L)}$_2$]$^+$ and [Dy^{III}{Ni^{II}(L')}$_2$]$^+$, respectively. Therefore, it appears that it is primarily the difference in the ligand field around the lanthanide(III) ion that leads to the striking differences in the magnetic properties.

We therefore have also performed an ab initio quantum chemical analysis for [Dy^{III}{Ni^{II}(L')}$_2$]$^+$ (see Table 4). This is based on the published structural parameters[59] and details are given as Supporting Information. It emerges that the changes in the ligand field around Dy^{III} lead to a significant increase of the axiality of the Dy^{III} center, well seen in the g tensor parameters of the ground state Kramers doublet, a much increased barrier to the first excited state Kramers doublet and a much higher contribution of the highest m_J term (15/2) to the lowest energy Kramers doublet. The fact that the precise correlation between the structural and electronic parameters is not entirely clear indicates how difficult it is to optimize such a magnet – specifically also with lanthanides, where coordination geometries are not easy to predict.[11,12,28] What is impressive and pleasing, however, is that the ab ignition quantum mechanical scheme used here is able to accurately predict the subtle differences in magnetic properties.

Conclusion

We have used an extensive ab initio quantum chemical analysis based on a CASSCF wavefunction, explicit spin-orbit coupling via the restricted space state interaction method (RASSI-SO) and a ligand field analysis, using the Lines model and Stevens operators, to predict the magnetic anisotropy of the two linear heterotrinuclear complexes [Dy^{III}{Ni^{II}(L)}$_2$]$^+$ and [Dy^{III}{Ni^{II}(L')}$_2$]$^+$ with the structurally related ligands L and L', both enforcing a distorted trigonal prismatic hexacoordinate Dy^{III} center with two slightly distorted octahedral Ni^{II} end groups. The single crystal molecular structures show that these two complexes are very similar with a small change of the ligand field around the Dy^{III} center as the main difference. The computed electronic properties confirm the experimental magnetic data, i.e., the effective barriers of magnetization relaxation are drastically different: while [Dy^{III}{Ni^{II}(L)}$_2$]$^+$ does not show SMM behavior, the very similar [Dy^{III}{Ni^{II}(L')}$_2$]$^+$ complex is an SMM with an effective barrier of 9.85 cm^{-1}.[59] This is important support for the validity of the theoretical setup used for the prediction of effective relaxation barriers in this class of molecules.

The computed electronic properties of [Dy^{III}{Ni^{II}(L)}$_2$]$^+$ are validated with experimental data based on SQUID magnetometry and paramagnetic NMR spectroscopy,[36] as well as single crystal DC-SQUID and HF-EPR data. Importantly, we are able to show that the ab initio calculated magnetic anisotropy of [Dy^{III}{Ni^{II}(L)}$_2$]$^+$ of $D^{calc} = -6.7$ cm^{-1} is in excellent agreement with that determined by NMR spectroscopy of $D^{exp} = -5.0$ cm^{-1}. In addition to previous similar studies, where we have used HF-EPR and magnetic circular dichroism (MCD) spectroscopy, together with an extensive ligand field analysis,[32,33] the entire set of experimental data presented here gives us confidence that the theoretical setup used can accurately predict the electronic and magnetic properties of oligonuclear 3d–4f complexes.

While the analysis of the EPR data does not yield overall molecular anisotropy parameters, it is illustrative to compare the computed parameters of Ni^{II} obtained from the calculations of the [(Lu^{III}){(Ni^{II})(Zn^{II})(L)$_2$}]$^+$ fragments with the experimental results. The calculations yield $D_{Ni} = +2.54$ and $+2.74$ cm^{-1} as well as $E_{Ni} = -0.74$ and -0.05 cm^{-1} (see Supporting Information, Table S8). While the signs of D and E from the calculations are

Table 4. Comparison [(Dy){(Ni)$_2$(L)$_2$}]$^+$ and [(Dy){(Ni)$_2$(L')$_2$}]$^+$ (parameters or the latter are in italics). The data given include the energies of the Kramers doublets and g tensor parameters as well as details of the wavefunction of the Kramers doublet 1 (ab initio calculations), parameters of the shape and twist angle analysis (see also Supporting Information).

Kramers doublet	RASSI energies [cm^{-1}]		g_X		g_Y		g_Z	
1	0.00	*0.00*	0.15	*0.00*	0.49	*0.00*	14.82	*19.66*
2	28.13	*91.54*	0.11	*0.00*	0.37	*0.01*	16.04	*17.37*
3	68.32	*122.78*	0.09	*0.05*	0.44	*0.11*	12.16	*15.16*
4	180.46	*189.96*	0.30	*0.02*	0.34	*0.12*	18.76	*11.85*
5	194.74	*295.12*	2.87	*4.35*	3.58	*4.43*	9.83	*7.87*
6	351.47	*484.51*	5.86	*3.99*	5.57	*4.63*	1.13	*5.29*
7	484.62	*644.67*	4.73	*0.41*	4.09	*0.84*	0.02	*4.30*
8	564.24	*747.68*	12.74	*11.18*	8.09	*9.70*	1.13	*1.14*
composition of KD 1	0.64|±13/2> +0.31|±9/2>		*0.98|±15/2>*					
anisotropy D	−6.7		*−11.6587*					
E	0.45		*0.0910*					
shape analysis								
Dy O$_h$	7.466		*7.887*					
Dy TP	4.759		*11.037*					
Dy Φ, d	31, 3.29		*48, 3.67*					
Ni O$_h$	1.026; 1.118		*1.273; 1.339*					
Ni TP	11.219; 10.666		*11.846; 11.848*					
Ni Φ, d	50, 2.64		*50, 2.57*					

Chemistry–A European Journal

Full Paper
doi.org/10.1002/chem.202100626

Chemistry Europe
European Chemical
Societies Publishing

opposite to the experimental parameters ($D_{Ni} = -1.5(2)$ cm^{-1}, $E_{Ni} = 0.5(1)$ cm^{-1}), the magnitude of the parameters are similar in order.[60] Specifically, the ratio of the anisotropy parameters, $E/D \sim 1/3$, is comparable. We also note that the isotropic g values of the Ni^{II} ions agree by experiments and calculations.

As mentioned before, the ab initio method used here to compute magnetic anisotropies is not undisputed.[24,33] Together with our earlier similar studies,[32,33] for three series of homo- and hetero-di- and tri-nuclear 3d–4f complexes, we find excellent agreement between the ab initio computed electronic/magnetic properties, specifically the magnetic anisotropies, and experimental data, including SQUID measurements, MCD, HF-EPR and paramagnetic NMR, and also including an extensive ligand field analysis. One important advantage of the ab initio in comparison with ligand field calculations is that, in principle, these may be used for predictions in addition to interpretations, *i.e.* for the "rational design" of new materials. Ligand field based methods have the disadvantage that transferability of ligand field parameters is questionable,[–61,66-68] although for transition metal complexes, it has been demonstrated that the errors resulting from assuming transferability are very small.[62]

Experimental Section

Materials: Syntheses, structures, powder SQUID and paramagnetic NMR experiments and analyses have been described previously.[36]

Crystallography: Two structures of the [Dy^{III}{Ni^{II}(L)}$_2$]$^+$ molecular cation have been reported ([Dy^{III}{Ni^{II}(L)}$_2$](ClO$_4$)·MeOH and [Dy^{III}{Ni^{II}(L)}$_2$](ClO$_4$). Deposition numbers 1458681 and 1458682 contain the supplementary crystallographic data for this paper. These data are provided free of charge by the joint Cambridge Crystallographic Data Centre and Fachinformationszentrum Karlsruhe Access Structures service. The published powder SQUID data were from the former structure with a molecule of MeOH of crystallization,[36] while the single crystal SQUID and HF-EPR measurements reported here are from the latter, MeOH-free structure; the quantum-chemical calculations were done for both structures (see Supporting Information). The single Crystal of [Dy^{III}{Ni^{II}(L)}$_2$][ClO$_4$] was oriented on an Agilent Technologies Supernova-E 4-circle CCD diffractometer using Mo Kα X-radiation. A complete set of intensity data was then collected with the same crystal. The structure was solved by the heavy atom method and could be refined surprisingly well despite the problems[69] that go along with the highly focused microsource beam and the strongly anisotropic morphology of the large crystal plate. The resulting structure was identical with that of the previously published solvent-free DyNi$_2$ complex.[36]

Static magnetic properties of a single crystal of the [Dy^{III}{Ni^{II}(L)}$_2$]$^+$ *complex* have been measured by means of a Quantum Design MPMS XL-5 SQUID magnetometer. For the measurements the oriented single crystal sample was fixed with low temperature varnish glue. The temperature dependence of the DC magnetic susceptibility, i.e. $\chi(T) = M(T)/B$, was obtained in the temperature range of $T = 2$–300 K at $B = 0.5$ T. The field dependence of the magnetization at $T = 2$ K was measured in the magnetic field range of $-5 \leq T \leq B \leq 5$ T. The temperature independent diamagnetic contribution of the complex χ_0 was subtracted from the experimental data using Pascal's constants.[70]

High-frequency electron paramagnetic resonance (HF-EPR) measurements were carried out on the single crystal in the frequency range 80 to 450 GHz, and between 2 and 30 K. As both source and detector of frequency-stabilized microwaves, a phase-sensitive millimeter-wave vector network analyzer (MVNA) from AB Millimetré was used. A superconducting magnet from Oxford provides magnetic fields of up to 16 T. For the measurements, the oriented single crystal was fixed with low temperature silicon grease in the sample space of the home-built transmission-type probe.[33]

Supporting Information

The Supporting Information includes details of the quantum chemical calculations, HF-EPR spectroscopy, and the paramagnetic NMR spectroscopy.

Conflict of Interest

The authors declare no conflict of interest.

[1] T. Lis, *Acta Crystallogr. Sect. B* **1980**, *36*, 2042.
[2] R. Sessoli, D. Gatteschi, A. Caneschi, M. A. Novak, *Nature* **1993**, *365*, 141–143.
[3] R. Sessoli, H.-L. Tsai, A. R. Schake, S. Wang, J. B. Vincent, K. Folting, D. Gatteschi, G. Christou, D. N. Hendrickson, *J. Am. Chem. Soc.* **1993**, *115*, 1804–1816.
[4] L. Bogani, W. Wernsdorfer, *Nat. Mater.* **2008**, *7*, 179–186.
[5] M. Manoli, A. Collins, S. Parsons, A. Candini, M. Evangelisti, E. K. Brechin, *J. Am. Chem. Soc.* **2008**, *130*, 11129.

Chemistry–A European Journal

Full Paper
doi.org/10.1002/chem.202100626

Chemistry Europe
European Chemical
Societies Publishing

[6] M. N. Leuenberger, D. Loss, *Nature* **2001**, *410*, 789–793.

[7] C. R. Ganivet, B. Ballesteros, G. de la Torre, J. M. Clemente-Juan, E. Coronado, T. Torres, *Chem. Eur. J.* **2013**, *19*, 1457.

[8] Y.-C. C. J. Liu, J.-L. Liu, V. Vieru, L. Ungur, J.-H. Jia, L. F. Chibotaru, Y. Lan, W. Wernsdorfer, S. Gao, X.-M. Chen, M.-L. Tong, *J. Am. Chem. Soc.* **2016**, *138*, 5441–5450.

[9] R. Sessoli, D. Gatteschi, *Angew. Chem. Int. Ed.* **2003**, *42*, 268–297; *Angew. Chem.* **2003**, *115*, 278.

[10] T. Glaser, *Chem. Commun.* **2011**, *47*, 116–130.

[11] M. Atanasov, P. Comba, S. Hausberg, B. Martin, *Coord. Chem. Rev.* **2009**, *253*, 2306–2314.

[12] P. Comba, M. Kerscher, *Coord. Chem. Rev.* **2009**, *253*, 564–574.

[13] F. Neese, D. A. Pantazis, *Faraday Discuss.* **2011**, *148*, 229–238.

[14] G. Aromi, E. K. Brechin, *Structure and Bonding, Vol. 122*, Springer-Verlag Berlin Heidelberg, **2006**, pp. 1–67.

[15] A. M. Akop, I. J. Hewitt, V. Mereacre, R. Clerac, W. Wernsdorfer, C. E. Anson, K. Powell, *Angew. Chem. Int. Ed.* **2006**, *45*, 4926; *Angew. Chem.* **2006**, *118*, 5170.

[16] J. D. Rinehart, J. R. Long, *Chem. Sci.* **2011**, *2*, 2078–2085.

[17] R. Sessoli, A. K. Powell, *Coord. Chem. Rev.* **2009**, *253*, 2328–2341.

[18] C. A. P. Goodwin, F. Ortu, D. Reta, N. F. Chilton, D. P. Mills, *Nature* **2017**, *548*, 439–442.

[19] F.-S. Guo, B. M. Day, Y.-C. Chen, M.-L. Tong, A. Mansikkamäki, R. A. Layfield, *Angew. Chem. Int. Ed.* **2017**, *56*, 11445–11449; *Angew. Chem.* **2017**, *129*, 11603.

[20] F.-S. Guo, B. M. Day, Y.-C. Chen, M.-L. Tong, A. Mansikkamäki, R. A. Layfield, *Science* **2018**, *362*, 1440–1403.

[21] S. Demir, M. I. Gonzalez, L. E. Darago, W. J. Evans, J. R. Long, *Nat. Commun.* **2017**, *8*, 2144.

[22] A. Ceulemans, L. F. Chibotaru, G. A. Heylen, K. Pierloot, L. G. Vanquickenborne, *Chem. Rev.* **2000**, *100*, 787–806.

[23] L. F. Chibotaru, L. Ungur, *J. Chem. Phys.* **2012**, *137*, 064112–064111–064112–064122.

[24] J. v. Leusen, M. Speldrich, H. Schilder, P. Kögerler, *Coord. Chem. Rev.* **2015**, *289–290*, 137–148.

[25] Y. Rechkemmer, J. E. Fischer, R. Marx, M. Dörfel, P. Neugebauer, S. Horvath, M. Gysler, T. Brock-Nannestad, W. Frey, M. F. Reid, J. v. Slageren, *J. Am. Chem. Soc.* **2015**, *157*, 13114–13120.

[26] T. Gupta, T. Rajeshkumar, G. Rajaraman, *Phys. Chem. Chem. Phys.* **2014**, *16*, 14568–14577.

[27] K. Ridier, B. Gillon, A. Gukasov, G. Chaboussant, A. Cousson, D. Luneau, A. Borta, J.-F. Jacquot, R. Checa, Y. Chiba, H. Sakiyama, M. Mikuriya, *Chem. Eur. J.* **2015**.

[28] K. Liu, W. Shi, P. Cheng, *Coord. Chem. Rev.* **2015**, *289–290*, 74–122.

[29] P.-A. Malmqvist, B. O. Roos, B. Schimmelpfennig, *Chem. Phys. Lett.* **2002**, *357*, 230–240.

[30] M. E. Lines, *J. Chem. Phys.* **1971**, *55*, 2977–2984.

[31] C. Rudowicz, *J. Phys. C* **1985**, *18*, 1415–1430.

[32] M. Bender, P. Comba, S. Demeshko, M. Großhauser, D. Müller, H. Wadepohl, *Z. Allg. Anorg. Chem., (Ekke Hahn Special Issue)* **2015**, 2291–2299.

[33] P. Comba, M. Großhauser, R. Klingeler, C. Koo, Y. Lan, D. Müller, J. Park, A. Powell, M. Riley, H. Wadepohl, *Inorg. Chem.* **2015**, *54*, 11247–11258.

[34] P. Comba, L. J. Daumann, R. Klingeler, C. Koo, M. J. Riley, A. E. Roberts, H. Wadepohl, J. Werner, *Chem. Eur. J. (Special Issue ECOSTBio)* **2018**, *24*, 5319–5330.

[35] P. Cieslik, P. Comba, W. Hergett, R. Klingeler, G. F. P. Plny, L. Spilleke, G. Velmurugan, *Z. Anorg. Allg. Chem. (Special Issue for P. Klüfers)* **2021**, *submitted*.

[36] P. Comba, M. Enders, M. Großhauser, M. Hiller, D. Müller, H. Wadepohl, *Dalton Trans.* **2017**, *46*, 138–149.

[37] F. Aquilante, L. De Vico, N. Ferré, G. Ghigo, P.-A. Malmqvist, P. Neogrády, T. B. Pedersen, M. Pitonak, M. Reiher, B. O. Roos, L. Serrano-Andrés, M. Urban, V. Veryazov, R. Lindh, *J. Comput. Chem.* **2010**, *31*, 224–247.

[38] B. O. Roos, R. Lindh, P.-A. Malmqvist, V. Veryazov, P.-O. Widmark, *J. Phys. Chem. A* **2004**, *108*, 2585.

[39] B. O. Roos, R. Lindh, P.-A. Malmqvist, V. Veryazov, P.-O. Widmark, *J. Phys. Chem. A* **2005**, *109*, 6575–6579.

[40] M. Damjanović, Y. Horie, T. Morita, Y. Horii, K. Katoh, M. Yamashita, M. Enders, *Inorg. Chem.* **2015**, *54*, 11986–11992.

[41] M. Damjanovic, K. Katoh, M. Yamashita, M. Enders, *J. Am. Chem. Soc.* **2013**, *135*, 14349–14358.

[42] I. Bertini, C. Luchinat, G. Parigi, *Prog. Nucl. Magn. Reson. Spectrosc.* **2002**, *40*, 249–273.

[43] I. Bertini, C. Luchinat, G. Parigi, E. Ravera, *Elsevier, Boston* **2017**.

[44] L. F. Chibotaru, L. Ungur, A. Soncini, *Angew. Chem. Int. Ed.* **2008**, *47*, 4126–4129; *Angew. Chem.* **2008**, *120*, 4194.

[45] L. Ungur, W. Van den Heuvel, L. F. Chibotaru, *New J. Chem.* **2009**, *33*, 1224–1230.

[46] L. F. Chibotaru, L. Ungur, C. Aronica, H. Elmoll, G. Pilet, D. Luneau, *J. Am. Chem. Soc.* **2008**, *130*, 12445–12455.

[47] L. Noodleman, *J. Chem. Phys.* **1981**, *74*, 5737.

[48] E. Ruiz, J. Cano, S. Alvarez, A. Caneschi, D. Gatteschi, *J. Am. Chem. Soc.* **2003**, *125*, 6791.

[49] P. Comba, S. Hausberg, B. Martin, *J. Phys. Chem. A* **2009**, *113*, 6751.

[50] S. K. Singh, N. K. Tibrewal, G. Rajaraman, *Dalton Trans.* **2011**, *40*, 10897–10906.

[51] V. S. Mironov, Y. G. Galyametdinov, A. Ceulemans, C. Görller-Warand, K. Binnemans, *J. Chem. Phys.* **2002**, *116*, 4673–4685.

[52] B. R. McGarvey, *J. Magn. Reson.* **1979**, *33*, 445–455.

[53] M. Gerloch, R. F. McMeeking, *J. Chem. Soc. Dalton Trans.* **1975**, 2443–2451.

[54] S. F. M. Schmidt, C. Koo, V. Mereacre, J. Park, D. W. Heermann, V. Kataev, C. E. Anson, D. Prodius, G. Novitchi, R. Klingeler, A. K. Powell, *Inorg. Chem.* **2017**, *56*, 4796–4806.

[55] J. Krzystek, A. Ozarowski, J. Telser, *Coord. Chem. Rev.* **2006**, *250*, 2308–2324.

[56] P. I. Feng, C. C. Beedle, C. H. Koo, W. Wernsdorfer, M. Nakano, S. Hill, D. N. Hendrickson, *Inorg. Chem.* **2008**, *47*, 3188–3204.

[57] N. Ahmed, C. Das, S. Vaidya, S. K. Langley, K. S. Murray, M. Shanmugam, *Chem. Eur. J.* **2014**, *20*, 14235–14239.

[58] A. Upadhyay, C. Das, S. K. Langley, K. S. Murray, A. K. Srivastava, M. Shanmugam, *Dalton Trans.* **2016**, *45*, 3616–3626.

[59] M.-X. Yao, Z.-X. Zhu, X.-Y. Lu, X.-W. Deng, S. Jing, *Dalton Trans.* **2016**, *45*, 10689–10695.

[60] Note that the experimentally determined D_{Ni} values are single-ion anisotropies (see eqn. 5 for the corresponding Hamiltonian) but the contribution of Dy^{III} is not properly included. Since the D_{zz} axes are not colinear (see Figure 1), the computed projection [$D = 1/6\,D_{Ni1} + 1/6\,D_{Ni2}$ ($+ 1/3\,D_{NiNi}$, omitted)] with $D = 0.9$ cm^{-1} is only a rough estimate but in the range of the experimental value ($D = -1.5$ cm^{-1}). Note also that the two D_{zz} directions are approx. perpendicular, and therefore it is not unexpected that the experimentally determined anisotropy is negative.

[61] H. Stratemeier, M. A. Hitchman, P. Comba, P. V. Bernhardt, M. J. Riley, *Inorg.Chem.* **1991**, *30*, 4088.

[62] P. V. Bernhardt, P. Comba, *Inorg. Chem.* **1993**, *32*, 2798–2803.

[63] P. Comba, *Inorg. Chem.* **1994**, *33*, 4577–4583.

[64] M. Llunell, D. Casanova, J. Cirera, P. Alemany, S. Alvarez, *SHAPE 2.1, SHAPE, Version 2.1*; Barcelona: 2013.

[65] P. Comba, *Inorg. Chem.* **1989**, *28*, 426.

[66] J. Glerup, O. Monsted, C. E. Schäffer, *Inorg. Chem.* **1980**, *19*, 2855.

[67] M. Gerloch, R. G. Woolley, *J. Chem. Soc., Dalton* **1981**, 1714.

[68] L. G. Vanquickenborne, B. Coussens, D. Postelmans, A. Ceulemans, K. Pierloot, *Inorg. Chem.* **1991**, *30*, 2978.

[69] L. Krause, R. Herbst-Irmer, G. M. Sheldrick, D. Stalke, *J. Appl. Cryst.* **2015**, *48*, 3–10.

[70] G. A. Bain, J. F. Berry, *J. Chem. Educ.* **2008**, *85*, 532.